Errors in the Measurement of Turbulence Upstream of an Axisymmetric Body

JOHN C. WYNGAARD AND LARRY ROCKWELL

National Center for Atmospheric Research, Boulder, CO 80307*

CARL A. FRIEHE

University of California, Irvine, Irvine, CA 92717

(Manuscript received 15 February 1985, in final form 6 May 1985)

ABSTRACT

We use a Taylor series expansion technique to calculate the effects of mean-flow distortion on turbulence measurements ahead of an axisymmetric body. The approach is valid when the integral scale of the turbulence is large compared to the maximum body diameter, which is usually the case for energy-containing turbulence statistics measured ahead of aircraft and the towed bodies used in oceanography. Using a 5:1 ellipsoid as a representative body, we show the nature of the attenuation and crosstalk error terms which the flow distortion induces in the measured turbulence components. The contours of the resulting errors in velocity covariances measured ahead of the ellipsoid and a paraboloid of revolution reveal that, in general, the errors in turbulent Reynolds stress can be the most severe. For sufficiently small distortion effects, which typically means more than one diameter away from the nose, the distortion matrix can easily be inverted analytically, giving explicit expressions for the true covariances in terms of the measured ones. We assess the effects of averaging measurements taken in different directions along the same path, as is sometimes done with aircraft data, and of nonzero angle of attack.

1. Introduction

Traditional *in-situ* sensors inevitably cause distortion of the velocity field being measured. In geophysical applications the measuring platform (e.g., aircraft, balloon, towed body, meteorological mast, buoy) also contributes to this distortion, which in severe cases can induce large errors in turbulence statistics. One of the most important such statistics is the Reynolds stress (Tennekes and Lumley, 1972) which in the atmospheric boundary layer is proportional to the covariance between vertical and horizontal velocity fluctuations.

In a pioneering paper on turbulence distortion by bluff bodies, Hunt (1973) showed that the effects are quite different in the limits $a/L_x \to 0$ and $a/L_x \to \infty$, where a is the body scale and L_x is the integral scale of the approaching turbulence. Since good experimental practice dictates that the size of probes and probe supports be minimized, and since geophysical turbulence tends to have large integral scales, its measurement almost always involves small values of a/L_x. As Hunt has shown, the turbulence distortion theory in this limit is simpler than that for $a/L_x \to \infty$, essentially because when a/L_x is small, oncoming turbulent eddies detour around the body without significant interaction with the mean strain rates induced by the body. In effect, the turbulent velocity field instantaneously obeys potential flow, which is relatively easy to calculate.

Wyngaard (1981a) presented an approach to the turbulence distortion problem for $a/L_x \to 0$ which, while equivalent to Hunt's, is simpler to apply. He used it to calculate the distortion in turbulent stress ahead of a cylinder and a sphere. In a second paper, Wyngaard (1981b) applied the method to axisymmetric bodies, and presented exploratory results for a paraboloid of revolution.

In this paper we extend these studies and calculate the response of turbulent stress and velocity variances ahead of two types of axisymmetric bodies for the case $a/L_x \to 0$. This has relevance to the measurement of turbulence from a gust probe on the nose boom of aircraft and ahead of towed bodies, which are used frequently in oceanography.

2. Outline of the theory

The theory underlying our approach has been developed in detail by Wyngaard (1981a,b), but we will describe it briefly here.

Hunt (1973) has shown that for turbulent approach flow with $a/L_x \to 0$, the velocity field ahead of the body can be considered irrotational and steady. Wyngaard (1981a) has argued that this is true even if the undisturbed flow carries mean shear and turbulent shear

* The National Center for Atmospheric Research is sponsored by the National Science Foundation.

stress. Thus one can calculate the distorted flow with potential flow techniques. We assume that the distorted flow field $\tilde{U}_i(x)$ ahead of the body, having a mean part $\tilde{\bar{U}}_i$ and a turbulent part $\tilde{u}_i$, is an analytic function of the undistorted upstream flow:

$$\tilde{U}_i = \tilde{\bar{U}}_i + \tilde{u}_i = \tilde{U}_i[\mathbf{x}, U_1 + u_1(t), u_2(t), u_3(t)]. \quad (1)$$

Expanding (1) in a Taylor series about the basic state of unidirectional upstream flow, i.e., about $U_i = (U_1, 0, 0)$, yields an expression for the distorted turbulence field. To first order this gives

$$\tilde{u}_i(\mathbf{x}, t) = a_{i1}(\mathbf{x})u_1(t) + a_{i2}(\mathbf{x})u_2(t) + a_{i3}(\mathbf{x})u_3(t)$$
$$= a_{ij}(\mathbf{x})u_j(t). \quad (2)$$

We use the convention that repeated indices are summed. The matrix a_{ij} is defined by

$$a_{ij}(x) = \left.\frac{\partial \tilde{U}_i(\mathbf{x})}{\partial U_j}\right|_0, \quad (3)$$

where the subscript 0 refers to the basic state.

One can show that the second-order terms in the Taylor series expansion for $\tilde{u}_i(\mathbf{x}, t)$ are of order u/V relative to the leading terms, where u is the root-mean-square turbulent velocity and V is the mean speed of the approach flow. If $u/V \ll 1$, which is the case in aircraft applications, we need retain only the linear terms in this expansion; thus we will work with the linear form (2).

In the absence of the body there is no flow distortion, so that $u_i(\mathbf{x}, t) = u_i(t)$; thus $a_{ij} = \delta_{ij}$, as can be seen from (2). When a body distorts the flow a_{ij} is no longer diagonal, so that "crosstalk" is induced among the turbulence components. Thus we express the a_{ij} as

$$a_{ij}(\mathbf{x}) = \delta_{ij} + d_{ij}(\mathbf{x}), \quad (4)$$

where $d_{ij} \to 0$ as flow-distortion effects vanish. We will call d_{ij} the flow-distortion matrix.

Crosstalk effects are particularly important for shear stress, say $\overline{u_1 u_3}$. Ahead of a two-dimensional body, for example, (2) and (4) indicate that the distorted turbulence components are

$$\tilde{u}_1 = (1 + d_{11})u_1 + d_{13}u_3, \quad (5)$$

$$\tilde{u}_3 = d_{31}u_1 + (1 + d_{33})u_3. \quad (6)$$

Multiplying and averaging gives an expression for stress in the region of flow distortion. To first order, this expression is

$$\overline{\tilde{u}_1\tilde{u}_3} = d_{31}\overline{u_1^2} + (1 + d_{11} + d_{33})\overline{u_1 u_3} + d_{13}\overline{u_3^2}. \quad (7)$$

Equation (7) indicates that crosstalk (through the d_{31} and d_{13} terms) will cause a stress to be measured ahead of the body even in the absence of stress in the free stream. There are also attenuation and amplification effects if $d_{11} + d_{33}$ does not vanish. The resulting errors in measured stress can be quite large if $\overline{u_1^2}$ and $\overline{u_3^2}$ are much larger than $|\overline{u_1 u_3}|$; that is, if the correlation coefficient between u_1 and u_3 is small. In the atmospheric surface layer it is seldom larger than 0.3 (Haugen *et al.*, 1971), and it can be much smaller in very convective conditions. Wyngaard (1981a) has calculated the flow-distortion matrix for a circular cylinder (with and without a wake) and for a wakeless sphere, and shown the nature of the errors in the stress measured ahead of these bodies.

3. Distortion by axisymmetric bodies

Figure 1 shows the two bodies for which we will present calculations. The paraboloid of revolution is the surface defined by rotating the curve

$$2x_3 = D[1 - (2x_1/L)^2] \quad (8)$$

about the x_1 axis. The ellipsoid is generated by similarly rotating the curve

$$x_1^2/(L/2)^2 + x_3^2/(D/2)^2 = 1. \quad (9)$$

In each case D is the maximum diameter of the body and L is its length. We will refer to L/D as the fineness ratio of the body.

For an axisymmetric body whose axis is along the x_1-direction (Fig. 1), and whose approach flow is also along the axis, symmetries reduce the number of independent elements in the flow-distortion matrix. Using $x_3 = r\cos\omega$ and $x_2 = -r\sin\omega$, we note that

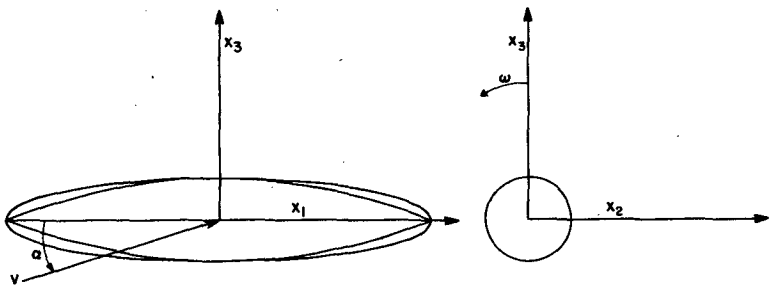

FIG. 1. Our coordinate system, and cross sections of the ellipsoid and paraboloid of revolution.

$$d_{21} = -T(r)\sin\omega, \tag{10}$$

$$d_{31} = T(r)\cos\omega, \tag{11}$$

where $T(r)$ is a function to be determined. Similarly, we see that

$$d_{12}(x_1, r, \omega) = d_{13}(x_1, r, \omega + \pi/2), \tag{12}$$

$$d_{22}(x_1, r, \omega) = d_{33}(x_1, r, \omega + \pi/2), \tag{13}$$

$$d_{32}(x_1, r, \omega) = -d_{23}(x_1, r, \omega + \pi/2), \tag{14}$$

because of axisymmetry. As a result of (10)–(14), the flow distortion matrix has only five independent elements.

The off-diagonal elements have an additional symmetry. One can see from the definition (3) of the a_{ij} that with axial flow approaching an axisymmetric body, the off-diagonal elements are zero at the origin.

We will next discuss the potential flow calculation techniques we used to determine the flow-distortion matrix, and then show the behavior of the elements (we will call them coefficients) in that matrix.

a. *The panel method*

We used the "panel method", in which the disturbance velocity potential is written as (Hess, 1975; Norment, 1980):

$$\phi(\mathbf{x}) = \int\int_S \frac{1}{|\mathbf{x} - q|}\,\sigma(q)dS, \tag{15}$$

where $\sigma(q)$ is the distribution of source strengths over the surface S. Figure 2 shows a panel model of a sphere.

The panel method yields the velocity field, which we must then differentiate with respect to the oncoming flow vector to obtain the flow-distortion matrix. We do this differentiation numerically, using the flow fields generated for varying approach flow velocities.

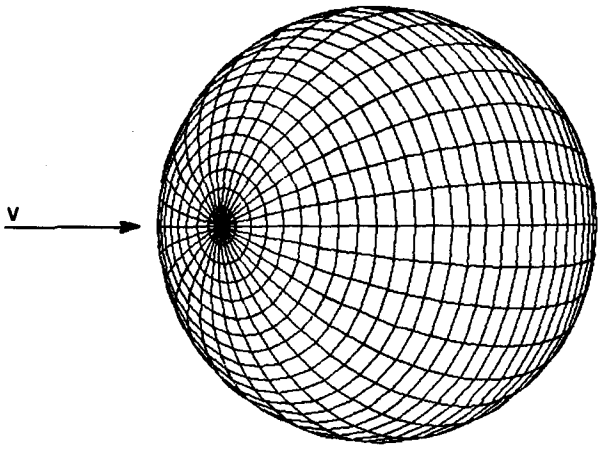

FIG. 2. A 1152-panel model of a sphere.

TABLE 1. Panelled sphere vs exact solution at $x_1 = -0.5D$.

Distortion coefficient	Average percent error: 256 panels	Average percent error: 1152 panels
d_{11}	0.1	0.1
d_{21}	2.8	2.1
d_{13}	2.6	1.9
d_{23}	4.8	2.7
d_{33}	5.4	3.0

Wyngaard (1981a) calculated exactly the flow-distortion matrix for a sphere, so we used these results to test and evaluate the panel method. We found that the flow-distortion matrix provided a more demanding test than the velocity field itself. The results for the five independent elements of the flow-distortion matrix are shown in Table 1. These results are averaged over a square of side one diameter, located 0.5 diameter upstream. Note that the average fractional errors in the coefficients determined with the panel method are of the order of a few percent for the 1152-panel calculation. We judged this to be a good compromise between accuracy and computational cost.

b. *Slender-body theory*

What is called "slender-body theory" is attractive in this application because it yields analytical expressions for the elements in the flow-distortion matrix. In this approach (Laitone, 1947a,b), one writes the distorted flow field ahead of a slender, axisymmetric body as

$$\tilde{U}_i = U_i + \frac{\partial\phi_1}{\partial x_i} + \frac{\partial\phi_2}{\partial x_i}, \tag{16}$$

where ϕ_1 and ϕ_2 are the disturbance velocity potentials for "thickness" and "angle-of-attack" effects, respectively:

$$\phi_1(\mathbf{x}) = \frac{-V}{4\pi}\int_0^L \frac{S'(\zeta)d\zeta}{[(x_1 - \zeta)^2 + r^2]^{1/2}} \tag{17}$$

$$\phi_2(\mathbf{x}) = \frac{Vx_3\sin\alpha}{2\pi}\int_0^L \left\{ \frac{S(\zeta)d\zeta}{[(x_1 - \zeta)^2 + r^2]^{3/2}} - \frac{S(\zeta)S''(\zeta)\ln\left(\frac{S(\zeta)}{\pi L^2}\right)}{4\pi[(x_1 - \zeta)^2 + r^2]^{3/2}} \right\} d\zeta. \tag{18}$$

Here V is the approach flow speed; α, the angle of attack, is the angle between the approach flow (assumed to be in the x_1–x_3 plane) and the body axis; S represents the cross-sectional area as a function of axial distance: and primes denote derivatives. Hence, the distorted velocity field is

$$\tilde{U}_1 = U_1 + V[I_1(\mathbf{x}) + I_2(\mathbf{x}) \sin\alpha], \quad (19)$$

$$\tilde{U}_2 = U_2 + V[I_3(\mathbf{x}) + I_4(\mathbf{x}) \sin\alpha], \quad (20)$$

$$\tilde{U}_3 = U_3 + V[I_5(\mathbf{x}) + I_6(\mathbf{x}) \sin\alpha], \quad (21)$$

where the I_i are the integrals given in the Appendix.

The symmetries (10)–(14) imply that at zero angle of attack we need compute only five flow-distortion coefficients, which we will take as d_{11}, d_{21}, d_{13}, d_{23}, and d_{33}. To generate these we need to differentiate the distorted velocity field with respect to the free-stream components U_1 and U_3. Since the slender-body expressions (17)–(21) are written in terms of free-stream speed and angle of attack, we use the chain rule in the forms

$$\left(\frac{\partial}{\partial U_1}\right)_{U_3} = \cos\alpha \left(\frac{\partial}{\partial V}\right)_{\alpha} - \frac{\sin\alpha}{V}\left(\frac{\partial}{\partial \alpha}\right)_{V}, \quad (22)$$

$$\left(\frac{\partial}{\partial U_3}\right)_{U_1} = \frac{\cos\alpha}{V}\left(\frac{\partial}{\partial \alpha}\right)_{V} + \sin\alpha \left(\frac{\partial}{\partial V}\right)_{\alpha}. \quad (23)$$

Note that at zero angle of attack the second term on the right sides of (22) and (23) vanishes. Having (19)–(23), we can now write the flow-distortion coefficients as

$$d_{11} = I_1 \cos\alpha, \quad (24)$$

$$d_{21} = I_3 \cos\alpha, \quad (25)$$

$$d_{13} = I_2 + I_1 \sin\alpha, \quad (26)$$

$$d_{23} = I_4 + I_3 \sin\alpha, \quad (27)$$

$$d_{33} = I_6 + I_5 \sin\alpha, \quad (28)$$

where again the second term on the right vanishes at zero angle of attack.

We would expect slender-body theory to fail if applied to a body that is not slender. We found that to be the case for a sphere, for which we know the flow-distortion coefficients exactly. In order to determine the limits of its applicability we did a series of test calculations for ellipsoids of various fineness ratios, using the panel method as the standard. We used 1152 panels, the number we found to give acceptable accuracy for the sphere. Figure 3 shows a 5:1 ellipsoid with 1152 panels. We calculated the flow-distortion matrix with slender-body theory, and with the panel method, with the results summarized in Tables 2 and 3. Again, the fractional errors in the distortion coefficients are averaged over a square one diameter on a side. The results suggest that 10:1 ellipsoids can be treated adequately with slender-body theory, and that 1.25:1 bodies clearly cannot be. We suggest that a reasonable limit of applicability of slender-body theory to our flow-distortion calculations is a fineness ratio of 5:1.

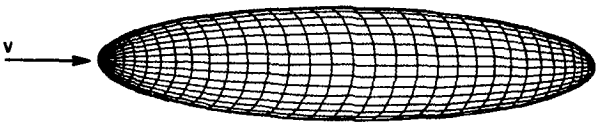

FIG. 3. A 1152-panel model of the 5:1 ellipsoid.

TABLE 2. Slender-body average percent deviation from panel model of ellipsoid at $x_1 = -0.5D$. Plus–minus values indicate one standard deviation.

Distortion coefficient	Fineness ratio 10/1	5/1	2.5/1	1.25/1
d_{11}	1.6 ± 1.0	3.1 ± 1.8	8.1 ± 4.1	20.9 ± 7.3
d_{21}	2.6 ± 1.5	3.9 ± 2.7	4.7 ± 3.9	8.7 ± 5.0
d_{13}	2.0 ± 1.5	2.2 ± 1.9	8.5 ± 3.8	55.8 ± 1.1
d_{23}	6.1 ± 2.2	8.1 ± 3.6	4.5 ± 3.2	53.2 ± 1.1
d_{33}	1.7 ± 1.2	4.1 ± 2.4	16.4 ± 3.9	58.5 ± 1.7

c. *The distortion coefficients*

We found that the coefficients varied considerably within the flow-distortion matrix, but that a given coefficient had qualitatively the same behavior for both bodies. Thus, the plots in Figs. 4 and 5, calculated for the 5:1 ellipsoid at 0.5 diameters upstream, are representative. These can be considered to be properties of the body, varying only with position upstream and being independent of mean flow speed (assuming it is large enough to minimize viscous effects, but not large enough to cause compressibility effects; that is, assuming the flow has a large Reynolds number and small Mach number).

Figures 4 and 5 confirm that the off-diagonal coefficients vanish on the axis. This is a general result for axisymmetric bodies, and an important one. It implies that crosstalk, which is the physical effect of the off-diagonal coefficients, vanishes along the axis. Note also from Figs. 4 and 5 that there is an order-of-magnitude variation in the values of the coefficients.

Having calculated the flow-distortion coefficients, we will next use them to calculate the errors induced in some important turbulence statistics.

TABLE 3. Slender-body average percent deviation from panel model of ellipsoid at $x_1 = -1.0D$. Plus–minus values indicate one standard deviation.

Distortion coefficient	Fineness ratio 10/1	5/1	2.5/1	1.25/1
d_{11}	2.9 ± 0.3	4.7 ± 0.6	10.6 ± 1.1	23.2 ± 1.8
d_{21}	0.3 ± 0.2	0.9 ± 0.6	5.1 ± 1.2	16.2 ± 1.9
d_{13}	0.5 ± 0.4	2.6 ± 0.6	14.2 ± 0.8	57.6 ± 0.3
d_{23}	2.2 ± 0.4	0.8 ± 0.6	9.9 ± 1.1	56.2 ± 0.7
d_{33}	1.6 ± 0.3	5.0 ± 0.5	17.5 ± 0.8	58.7 ± 0.4

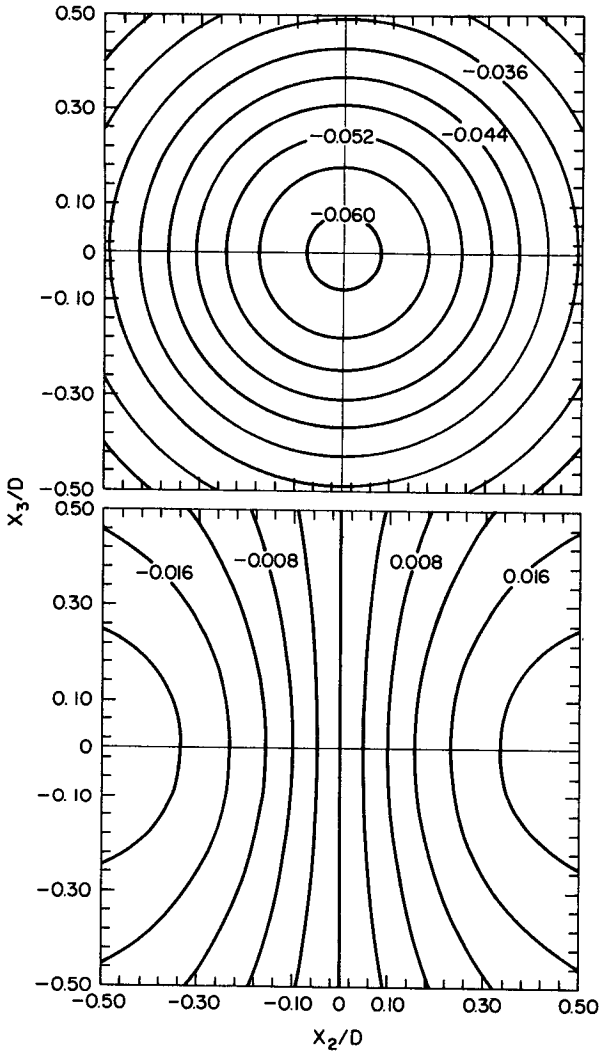

FIG. 4. Distortion coefficients in x_2–x_3 plane $0.5D$ ahead of a 5:1 ellipsoid; top, d_{11}, bottom, d_{21}.

4. Turbulence measurements ahead of axisymmetric bodies

a. The measured covariance

Equation (2) for the measured turbulence components implies that the measured velocity covariance is

$$\overline{\tilde{u}_i\tilde{u}_j} = a_{ik}a_{jm}\overline{u_k u_m}. \tag{29}$$

Expanding (29) for two components gives

$$\overline{\tilde{u}_1^2} = a_{11}^2\overline{u_1^2} + a_{12}^2\overline{u_2^2} + a_{13}^2\overline{u_3^2} + 2a_{12}a_{11}\overline{u_1u_2} + 2a_{11}a_{13}\overline{u_1u_3} + 2a_{12}a_{13}\overline{u_2u_3}, \tag{30}$$

$$\overline{\tilde{u}_1\tilde{u}_3} = a_{11}a_{31}\overline{u_1^2} + a_{12}a_{32}\overline{u_2^2} + a_{13}a_{33}\overline{u_3^2} + (a_{11}a_{32} + a_{12}a_{31})\overline{u_1u_2} + (a_{11}a_{33} + a_{13}a_{31})\overline{u_1u_3} + (a_{12}a_{33} + a_{13}a_{32})\overline{u_2u_3}. \tag{31}$$

Note that in each case the measured property is contaminated by a combination of attenuation and cross-talk effects. Along the axis of symmetry, however, the

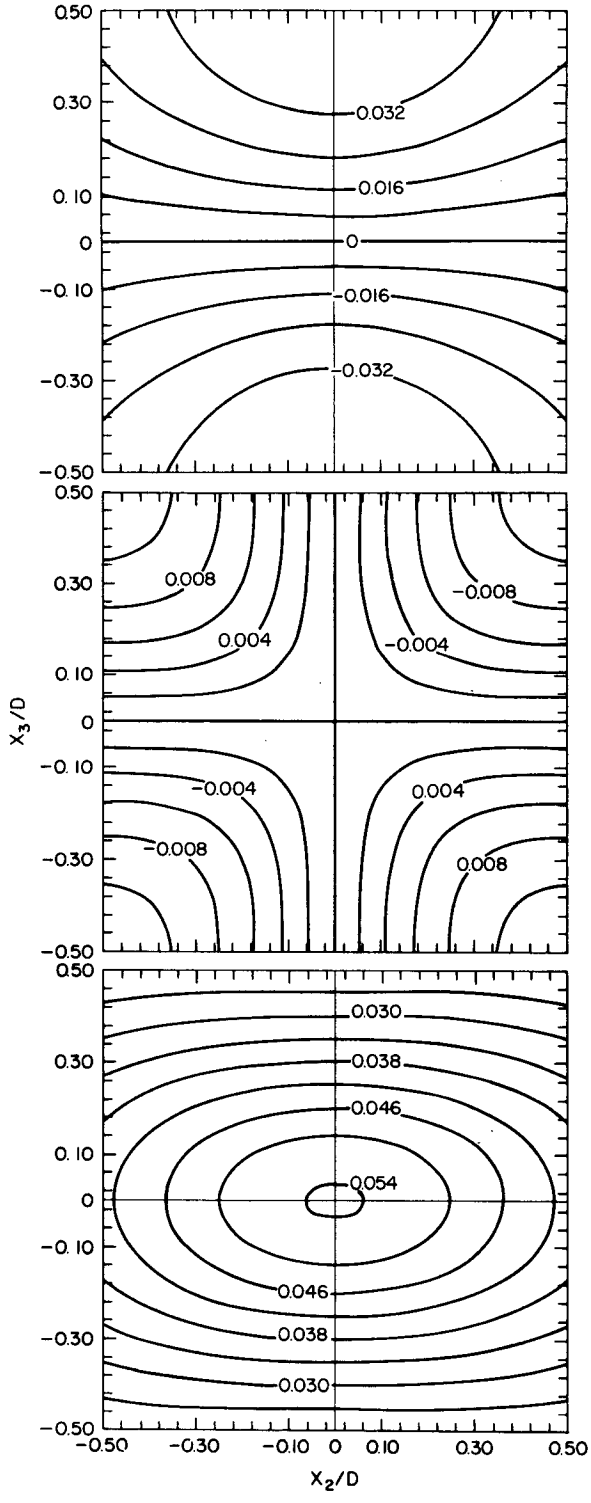

FIG. 5. As in Fig. 4, except: top, d_{13}; middle, d_{23}; bottom, d_{33}.

TABLE 4. Freestream turbulence statistics used in calculations (arbitrary units).

Quantity	Value
$\overline{u_1^2}$	10
$\overline{u_2^2}$	10
$\overline{u_3^2}$	10
$\overline{u_1 u_3}$	1
$\overline{u_2 u_3}$	1
$\overline{u_1 u_2}$	1

crosstalk effects vanish, as we mentioned earlier, and the measured statistics suffer only attenuation.

To illustrate the nature and magnitude of the errors induced in turbulence statistics we have done calculations with the assumed set of freestream turbulence properties shown in Table 4. Since Eq. (29) for measured properties is linear, only the relative magnitudes in Table 4 are significant. The values we chose are consistent with those measured in the AMTEX experiment (Lenschow *et al.*, 1980) in the midregions of a convective boundary layer over water.

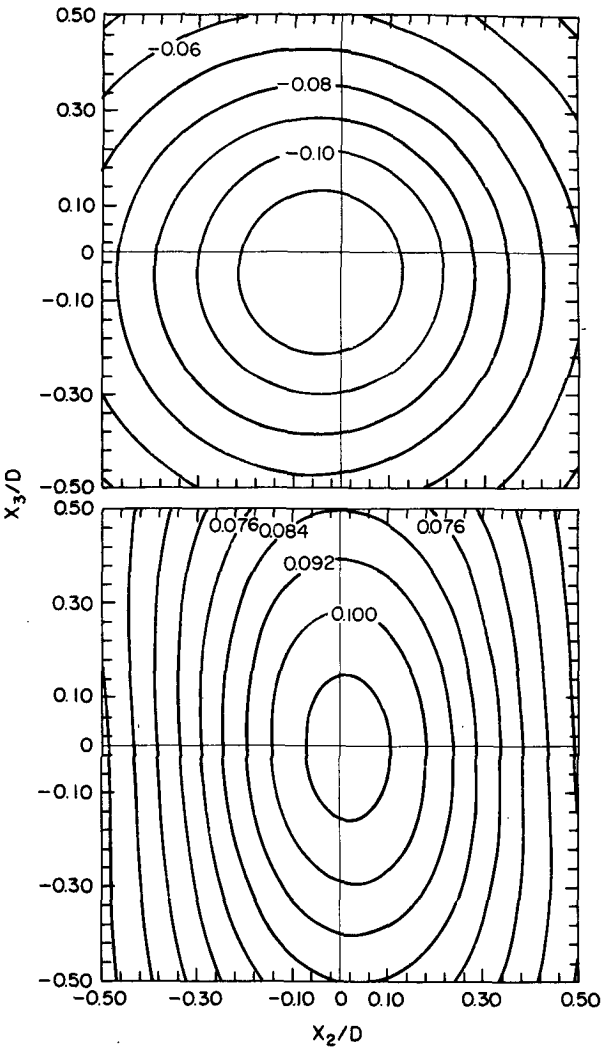

FIG. 6. Fractional errors in measured turbulence statistics in x_2–x_3 plane $0.5D$ ahead of a 5:1 ellipsoid. Top, $\tilde{u}_1^2$; bottom, $\tilde{u}_2^2$. Freestream statistics given in Table 4.

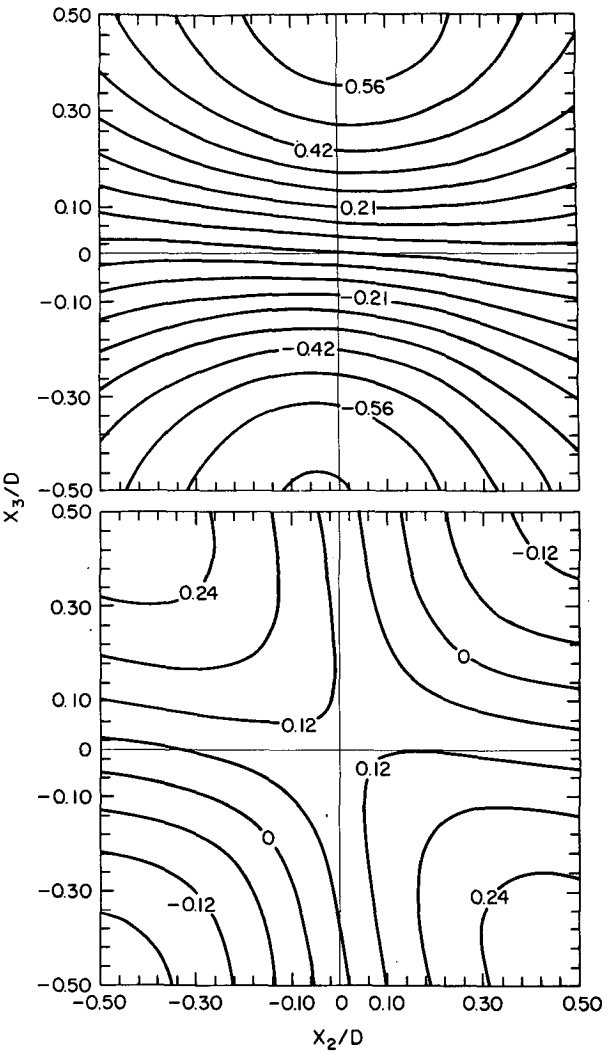

FIG. 7. As in Fig. 6 except: top, $\overline{\tilde{u}_1\tilde{u}_3}$; bottom, $\overline{\tilde{u}_2\tilde{u}_3}$.

We show the resulting plots of fractional error [i.e., (measured value − true value)/(true value)] in Figs. 6 and 7. Those plots, prepared for the plane 0.5 diameter ahead of the body, indicate that for the assumed turbulence levels, errors of the order of 10% or greater are induced in all statistics on the axis of symmetry. Errors off-axis can be larger or smaller, depending on the property in question.

Figure 8 contrasts the errors in $\overline{\tilde{u}_1\tilde{u}_3}$ and $\overline{\tilde{u}_2\tilde{u}_3}$ in a $D \times D$ square ahead of the two types of bodies, again for

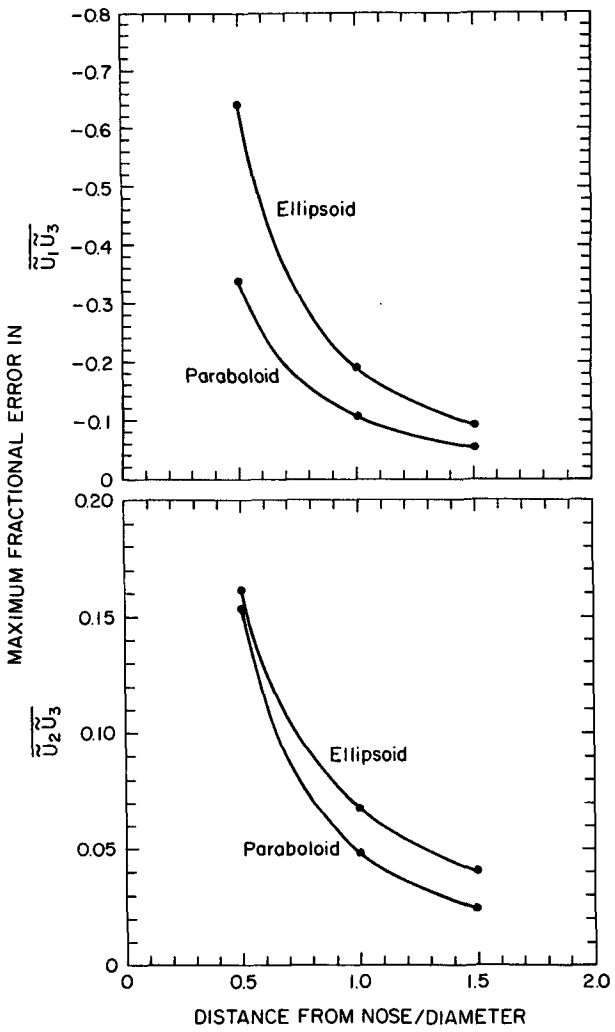

FIG. 8. Distortion error in $\overline{\tilde{u}_1\tilde{u}_3}$ (top) and $\overline{\tilde{u}_2\tilde{u}_3}$ (bottom) ahead of a 5:1 ellipsoid and a 5:1 paraboloid.

the set of freestream turbulence statistics in Table 4. The maximum errors occur off the axis, and for the assumed freestream conditions is negative for $\overline{\tilde{u}_1\tilde{u}_3}$ and positive for $\overline{\tilde{u}_2\tilde{u}_3}$. Note also that the errors for the paraboloid are appreciably less than for the ellipsoid, and that they decrease rapidly with distance from the body.

The distortion-induced crosstalk among velocity components causes stress to be measured even if there is none in the freestream flow. To illustrate this, we show in Fig. 9 the maximum induced stresses within a $D \times D$ square at locations ahead of the 5:1 ellipsoid. The maxima are located off-axis, of course, because, as we pointed out earlier, crosstalk vanishes on the axis of symmetry. In this calculation we set the off-diagonal components of $\overline{u_iu_j}$ to zero and used equal freestream variances; hence, in this case the induced stress distribution is symmetric in the x_2–x_3 plane, having positive and negative maxima of equal magnitudes which scale with the variance level in the freestream flow.

In the convective boundary layer the values of $\overline{u_1^2}$, $\overline{u_2^2}$, and $\overline{u_3^2}$ are of order $0.3w_*^2$ (Lenschow *et al.*, 1980) where w_* is the convective velocity scale. In clear, midday conditions over land w_* can easily be as large as 2.5 m s^{-1}, giving velocity variances on the order of 2 m^2 s^{-2}. For these conditions Fig. 9 indicates that spurious $\overline{u_2u_3}$ and $\overline{u_1u_3}$ values of the order of 200 and 600 cm^2 s^{-2}, respectively, would be measured 0.75 diameters ahead of a 5:1 ellipsoid. Because of the complicating effects of baroclinity and entrainment it is difficult to make any general statements about stress values in the convective boundary layer, but without these complications and with a 5 m s^{-1} mean wind over a typical rural surface, the stress magnitude decreases roughly linearly from about 1000 cm^2 s^{-2} at the surface to zero at the boundary-layer top. Clearly, then, there are conditions in which these spurious stresses could be significant.

b. Retrieving the true covariance

Our result (29) expresses the measured covariance in terms of the true one. However, in order to correct measurements for the distortion errors, we need the inverse relation:

$$\overline{u_iu_j} = a_{ik}^{-1}a_{jm}^{-1}\overline{\tilde{u}_k\tilde{u}_m}. \tag{32}$$

Here a^{-1} is the inverse of a, with the property

$$a_{ij}^{-1}a_{jk} = \delta_{ik}. \tag{33}$$

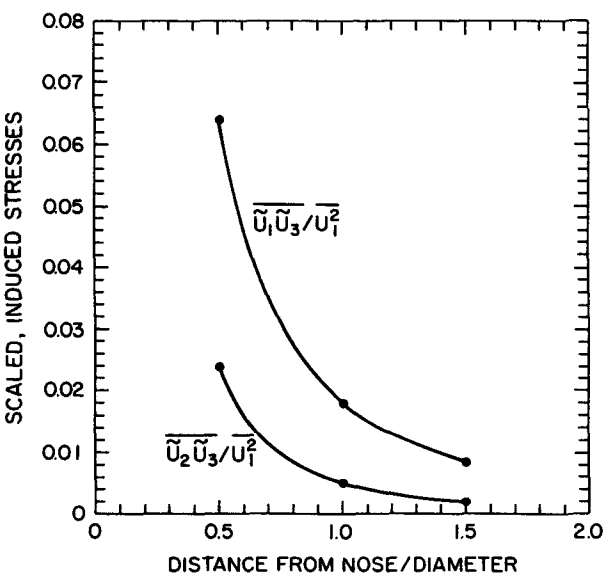

FIG. 9. Maximum induced stresses ahead of a 5:1 ellipsoid, scaled with freestream velocity variance. Off-diagonal components of $\overline{u_iu_j}$ are zero upstream; diagonal components are equal.

It follows that we can write each element of the true covariance $\overline{u_i u_j}$ as the product of a two-dimensional matrix and the measured covariance matrix. For example, the expression for the true stress $\overline{u_1 u_3}$ is

$$\overline{u_1 u_3} = a_{1k}^{-1} a_{3m}^{-1} \overline{\tilde{u}_k \tilde{u}_m} = S_{km} \overline{\tilde{u}_k \tilde{u}_m}, \quad (34)$$

and that for $\overline{u_2 u_3}$ is

$$\overline{u_2 u_3} = a_{2k}^{-1} a_{3m}^{-1} \overline{\tilde{u}_k \tilde{u}_m} = L_{km} \overline{\tilde{u}_k \tilde{u}_m}. \quad (35)$$

One can use standard matrix inversion routines to determine the inverse matrix numerically, given the values of the distortion coefficients. However, we can also do an approximate inversion analytically when the distortion coefficients are small, which is typically the case one diameter or so away from the body. In this case a_{ij} is only slightly different from δ_{ij}; this allows us to use a power series expansion for the inverse (Strang, 1976). Again, we keep only the linear term in the expansion:

$$\mathbf{a}^{-1} = \delta_{ij} - d_{ij} = \begin{vmatrix} 1 - d_{11} & -d_{12} & -d_{13} \\ -d_{21} & 1 - d_{22} & -d_{23} \\ -d_{31} & -d_{32} & 1 - d_{33} \end{vmatrix}. \quad (36)$$

The corresponding linearized expressions for S_{ij} and L_{ij} are

$$\mathbf{S} = \begin{vmatrix} -d_{31} & -d_{32} & 1 - d_{11} - d_{33} \\ 0 & 0 & -d_{12} \\ 0 & 0 & -d_{13} \end{vmatrix}, \quad (37)$$

$$\mathbf{L} = \begin{vmatrix} 0 & 0 & -d_{21} \\ -d_{31} & -d_{32} & 1 - d_{22} - d_{33} \\ 0 & 0 & -d_{23} \end{vmatrix}. \quad (38)$$

One can generate the matrices required for correction of other components of the measured covariance by using (32) and the linearized expression (36) for the inverse of a_{ij}.

These results allow one to extract the true covariance matrix very simply from measurements of its distorted components. To illustrate this, we used (34, 35) and (37, 38) to correct the values of the shear stress components measured $0.5D$ ahead of a 5:1 ellipsoid. Figure 7 shows the distorted stresses, and Fig. 10 shows the fractional errors remaining in their corrected values. Note that typically 90% or more of the distortion error is removed. Even less fractional error would remain at $1.0D$ ahead of the body, where the distortion coefficients are smaller and, hence, the linearized inversion of a_{ij} is more accurate.

5. Application to towed bodies and aircraft

The results in the previous section are indicative of the errors in turbulence statistics measured ahead of aircraft and towed bodies following straight, level paths at zero angle of attack. Let us now consider the effects of averaging measurements from runs in opposite directions, and the effects of nonzero angle of attack.

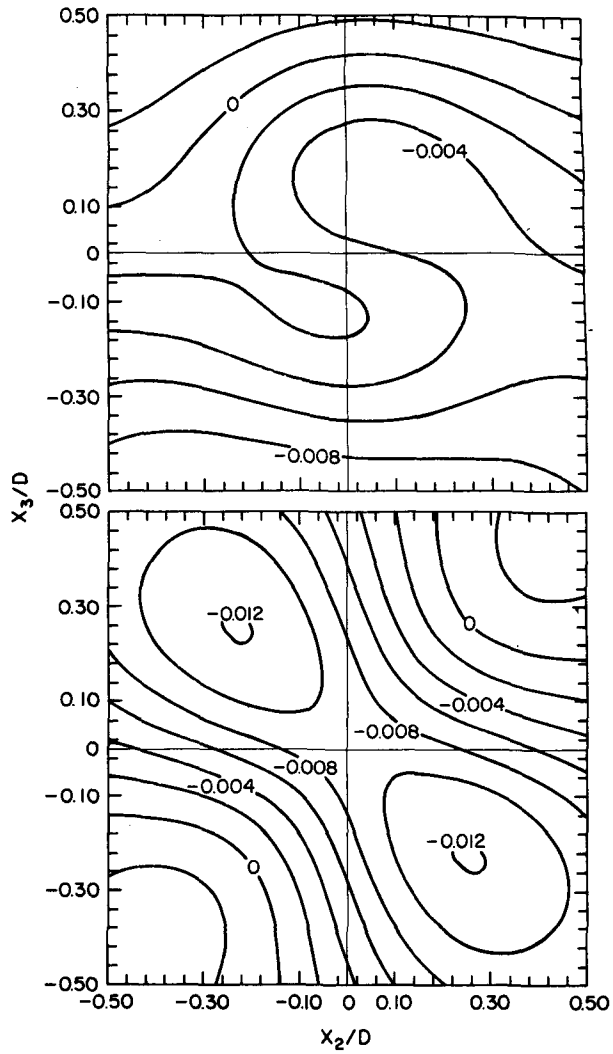

FIG. 10. Fractional errors remaining in $\overline{\tilde{u}_1 \tilde{u}_3}$ (top) and $\overline{\tilde{u}_2 \tilde{u}_3}$ (bottom) after using (34, 35) and (37, 38) to correct their measured values for flow-distortion effects.

a. *Reverse-heading effects*

Assume that turbulence measurements are made from a boom ahead of an axisymmetric aircraft, and that there are no sensor-induced measurement errors. We adopt the coordinate system shown in Fig. 1, with V being the speed of the air with respect to the aircraft and with the angle of attack α equal to zero. We assume that the motion of the aircraft coordinate system is simply a Galilean transformation of an earth-based

system; hence, Eq. (29) represents the measured turbulence statistics in earth coordinates.

If the aircraft flies in the opposite direction along the same flight path, its coordinate system is again a Galilean-transformed version of the earth-based one, but with the additional change of a reflection of the x_1 and x_2 axes. Thus, if the free-stream turbulence field is stationary and homogeneous, its statistical properties as seen in the aircraft coordinates will differ from those of the first flight path by the transformation $u_1 \rightarrow -u_1$, $u_2 \rightarrow -u_2$. It follows that the measured statistics in earth-based coordinates are given by (29) with the signs of u_1 and u_2 changed. If we then average the results from the two runs in opposite directions we obtain for $\widetilde{u_1^2}$ and $\widetilde{u_1 u_3}$, for example,

$$\widetilde{u_1^2} = a_{11}^2\overline{u_1^2} + a_{12}^2\overline{u_2^2} + a_{13}^2\overline{u_3^2} + 2a_{12}a_{11}\overline{u_1 u_2}, \quad (39)$$

$$\widetilde{u_1 u_3} = (a_{11}a_{33} + a_{13}a_{31})\overline{u_1 u_3} + (a_{12}a_{33} + a_{13}a_{32})\overline{u_2 u_3}. \quad (40)$$

Comparison of (39) and (40) with (30) and (31) shows that some of the spurious terms have been eliminated by the averaging of reverse-heading runs. Whether this reduces error depends on the instrument location and the freestream statistics.

b. Nonzero angle of attack

Aircraft typically fly at a few degrees angle of attack rather than zero, as we have assumed in our calculations up to this point. Slender-body theory can give us some insight into the effects of small angles of attack. Rewriting its predictions (24)–(28) by using the approximations $\cos\alpha \approx 1$, $\sin\alpha \approx \alpha$ gives:

$$d_{11}(\alpha) \approx d_{11}(0), \quad (41)$$

$$d_{21}(\alpha) \approx d_{21}(0), \quad (42)$$

$$d_{13}(\alpha) \approx d_{13}(0) + \alpha d_{11}(0), \quad (43)$$

$$d_{23}(\alpha) \approx d_{23}(0) + \alpha d_{21}(0), \quad (44)$$

$$d_{33}(\alpha) \approx d_{33}(0) + \alpha d_{31}(0). \quad (45)$$

This set indicates that the principal effect of a small angle of attack is to introduce new contributions to d_{i3}, $i = 1, 2, 3$. These new contributions are proportional to α, which usually does not exceed 0.05–0.10, and to other flow-distortion coefficients which, however, can be substantially larger than d_{i3}. Thus, it is possible that small angles of attack can have a detectable effect on turbulence statistics measured in some applications. We will discuss this in more detail in a forthcoming paper which deals specifically with aircraft applications.

6. Conclusions

Our study shows that flow distortion can induce significant errors in velocity covariances measured ahead of axisymmetric bodies. The errors depend on the flow-distortion matrix which relates the velocity field near the body to the free-stream velocity, but they also depend on the free-stream turbulence properties. We found a simple solution to the inverse problem of determining the true velocity covariances from their measured components.

We found that the slender-body approximation allows the flow-distortion matrix to be evaluated in closed form, but we found also that this approximation is not reliable for bodies of fineness ratio less than about 5:1. This approximation also shows that for slender bodies the flow-distortion matrix depends only weakly on angle of attack.

We found the panel method to be a good alternative to the slender-body theory in calculating the flow-distortion matrix for bodies that are not slender. While we used it only for axisymmetric bodies, given adequate computational resources one can easily extend it to complex shapes such as aircraft.

Acknowledgments. We are grateful to Hillyer Norment of Atmospheric Science Associates for providing us with his computer code for the panel method; to Warren King, Peggy LeMone, Don Lenschow, and Jack Warner for helpful discussions; and to Hope Hamilton for producing the manuscript.

CAF was supported by NCAR funds for a portion of this work, and by NSF Grant ATM-8318469.

APPENDIX

Integrals from Slender-Body Theory

$$I_1(\mathbf{x}) = \frac{1}{4\pi}\int_0^L \frac{S'(\zeta)(x_1-\zeta)d\zeta}{[(x_1-\zeta)^2+r^2]^{3/2}},$$

$$I_2(\mathbf{x}) = -\frac{x_3}{2\pi}\int_0^L \left(\frac{3(x_1-\zeta)S(\zeta)}{[(x_1-\zeta)^2+r^2]^{5/2}} - \frac{3(x_1-\zeta)S(\zeta)S''(\xi)\ln(S(\zeta)/\pi L^2)}{4\pi[(x_1-\zeta)^2+r^2]^{5/2}}\right)d\zeta,$$

$$I_3(\mathbf{x}) = \frac{1}{4\pi}\int_0^L \frac{S'(\zeta)x_2 d\zeta}{[(x_1-\zeta)^2+r^2]^{3/2}},$$

$$I_4(\mathbf{x}) = -\frac{x_3}{2\pi}\int_0^L \left(\frac{3x_2S(\zeta)}{[(x_1-\zeta)^2+r^2]^{5/2}} - \frac{3x_2S(\zeta)S''(\zeta)\ln(S(\zeta)/\pi L^2)}{4\pi[(x_1-\zeta)^2+r^2]^{5/2}}\right)d\zeta,$$

$$I_5(\mathbf{x}) = \frac{1}{4\pi}\int_0^L \frac{S'(\zeta)x_3 d\zeta}{[(x_1-\zeta)^2+r^2]^{3/2}}$$

$$I_6(\mathbf{x}) = -\frac{1}{2\pi}\left\langle x_3\int_0^L \left\{\frac{3x_3S(\zeta)}{[(x_1-\zeta)^2+r^2]^{5/2}}\right.\right.$$

$$- \frac{3x_3 S(\zeta) S''(\zeta) \ln(S(\zeta)/\pi L^2)}{4\pi[(x_1 - \zeta)^2 + r^2]^{5/2}} \Big\} d\zeta$$

$$+ \int_0^L \left\{ \frac{-S(\zeta)}{[(x_1 - \zeta)^2 + r^2]^{3/2}} \right.$$

$$\left. + \frac{S(\zeta) S''(\zeta) \ln(S(\zeta)/\pi L^2)}{4\pi[(x_1 - \zeta)^2 + r^2]^{3/2}} \right\} d\zeta \Bigg\rangle .$$

Here S is cross-sectional area, ζ axial coordinate, primes denote derivatives, and L is body length.

REFERENCES

Haugen, D. A., J. C. Kaimal and E. F. Bradley, 1971: An experimental study of Reynolds stress and heat flux in the atmospheric surface layer. *Quart. J. Roy. Meteor. Soc.*, **97**, 168–180.

Hess, J. L., 1975: Review of integral-equation techniques for solving potential-flow problems with emphasis on the surface-source method. *Comput. Methods Appl. Mech. Eng.*, **5**, 145–196.

Hunt, J. C. R., 1973: A theory of turbulent flow round two-dimensional bluff bodies. *J. Fluid Mech.*, **61**, 625–706.

Laitone, E. V., 1947a: The subsonic flow about a body of revolution. *Quart. Appl. Math.*, **5**, 227–231.

——, 1947b: The linearized subsonic and supersonic flow about inclined slender bodies of revolution. *J. Aero. Sci.*, **14**, 631–642.

Lenschow, D. H., J. C. Wyngaard and W. T. Pennell, 1980: Mean-field and second moment budgets in a baroclinic, convective boundary layer. *J. Atmos. Sci.*, **37**, 1313–1326.

Norment, H. G., 1980: Calculation of water-drop trajectories to and about arbitrary three-dimensional bodies in potential airflow. NASA CR 3291; NTIS #N80-28302.

Strang, G., 1976: *Linear Algebra and its Applications.* Academic Press, New York, 374 pp.

Tennekes, H., and J. L. Lumley, 1972: *A First Course in Turbulence.* M.I.T., 300 pp.

Wyngaard, J. C., 1981a: The effects of probe-induced flow distortion on atmospheric turbulence measurements. *J. Appl. Meteor.*, **20**, 784–794.

——, 1981b: The distortion of turbulent shear flow upstream of a body. *Proc. Third Symp. Turbulent Shear Flows,* Davis, Univ. of Cal., 19.6–19.9.